Enhancing Coronal Structures with the Fourier Normalizing-radial-graded Filter

Druckmüllerová, Hana; Morgan, Huw; Habbal, Shadia Rifai

Published in:
Astrophysical Journal

DOI:
10.1088/0004-637X/737/2/88

Publication date:
2011

Citation for published version (APA):
Druckmüllerová, H., Morgan, H., & Habbal, S. R. (2011). Enhancing Coronal Structures with the Fourier Normalizing-radial-graded Filter. *Astrophysical Journal*, *737*(2), 88. https://doi.org/10.1088/0004-637X/737/2/88

The Astrophysical Journal, 737:88 (10pp), 2011 August 20 doi:10.1088/0004-637X/737/2/88

ENHANCING CORONAL STRUCTURES WITH THE FOURIER NORMALIZING-RADIAL-GRADED FILTER

Hana Druckmüllerová[1], Huw Morgan[2], and Shadia R. Habbal[2]
[1] Institute of Mathematics, Faculty of Mechanical Engineering, Brno University of Technology, Technická 2, 616 69 Brno, Czech Republic; ydruck00@stud.fme.vutbr.cz
[2] Institute for Astronomy, University of Hawaii, 2680 Woodlawn Drive, Honolulu, HI 96 822, USA; hmorgan@ifa.hawaii.edu, shadia@ifa.hawaii.edu
Received 2011 April 6; accepted 2011 May 27; published 2011 August 8

ABSTRACT

Images of the corona have a high dynamic range which is excellent for quantitative photometric analysis. To understand the processes governing the solar corona, it is essential to have information about the absolute brightness as well as the underlying structure. However, due to the steep radial gradient of brightness in the images, and to the fact that structures closer to the solar disk have higher contrast than structures further from the disk, human vision cannot view the intricate structure of the corona in such images. The recently developed normalizing-radial-graded filter (NRGF) is an effective way for revealing the coronal structure. In this work, we present a more adaptive filter inspired by the NRGF, which we call the Fourier normalizing-radial-graded filter (FNRGF). It approximates the local average and the local standard deviation by a finite Fourier series. This method enables the enhancement of finer details, especially in regions of lower contrast. We also show how the influence of additive noise is reduced by a modification to the FNRGF. To illustrate the power of the method, the FNRGF is applied to images of emission from coronal forbidden lines observed during the 2010 July 11 total solar eclipse. It is also successfully applied to space-based observations of the low corona in the extreme ultraviolet and to white light coronagraph observations, thus demonstrating the validity of the FNRGF as a new tool that will help the interpretation of the information embedded in most types of coronal images.

Key words: Sun: corona – techniques: image processing

1. INTRODUCTION

Technological advances in imaging systems and the rapid advances in computing power are driving the field of solar image processing. The wide range of detectors used in astronomical imaging typically has a dynamic range of 16 or more bits per pixels. Composing more images with different exposure times enhances the dynamic range even further. However, there is neither a printing technique nor a screen or projector that is able to distinguish that many levels of brightness. As a result, we are unable to directly interpret the information contained in these observations. Examples of such observations are images of the solar corona, taken during total solar eclipses, or with coronagraphs, and extreme ultraviolet (EUV) or X-ray images from spacecraft. In practice therefore, it is necessary to use at least two images for analysis: the calibrated image with high dynamic range suitable for a quantitative photometric analysis and a processed image with the reduced dynamic range necessary for revealing the underlying coronal structure. Useful not only for studying the structures themselves, the latter image can also suggest what parts of the calibrated image are suitable for quantitative analysis. Without the processed image, the structures would remain hidden and unexplored. There are two inherent features that need to be considered to reveal the structures in images of the solar corona: (1) the steep radial gradient of brightness, and (2) the relative contrast of the coronal structures which decreases with height. To reveal coronal structure effectively, a method must remove or reduce the steep decrease in brightness and structure contrast with increasing distance from the Sun.

The techniques which remove the steep decrease of brightness of the solar corona are generally called radial-graded filters (RGF). Before the era of digital image processing, the RGF were implemented at the time of observation by means of mechanical, e.g., Owaki & Saito (1967), or optical tools, e.g., Newkirk & Harvey (1968). Another way is to compose images taken with different exposure times. Long exposure times capture the faint structures further from the solar disk, whereas short exposures capture bright structures close to the solar disk without saturation. The composed image has a very high dynamic range and further filters can be applied to decrease the steep radial gradient of brightness. One of the early methods of edge enhancement was introduced by Koutchmy et al. (1988). Espenak (2000) used a standard photoediting software for implementation of a filter which enhanced high spatial frequencies. More recently, Druckmüller et al. (2006) introduced the adaptive circular high-pass filter (ACHF) for processing total solar eclipse images. This approach enhances structures on higher spatial frequencies independent of their orientation. Byrne et al. (2009) analyzed series of images of coronal mass ejections (CMEs) by subtracting medians of images over a period of time and further spatial differencing based on wavelet decomposition.

The normalizing-radial-graded filter (NRGF) introduced by Morgan et al. (2006) solves this problem by segmenting the corona into narrow circular regions centered on the Sun, and calculating an average and standard deviation of brightness for each circular region. This approach gives a smooth profile of the average and standard deviation of brightness as a function of height within the image. Each pixel is then processed according to its height within the image by subtracting the average (thus removing the steep radial gradient) and dividing by the standard deviation (thus removing the radially decreasing brightness contrast). The NRGF is now a standard approach for processing coronal images, for example (Habbal et al. 2010a, 2010b), and has aided new insights into coronal structure and evolution (Morgan & Habbal 2007a, 2007b, 2010). Further examples of its application are given by He et al. (2009), Wang et al. (2010),

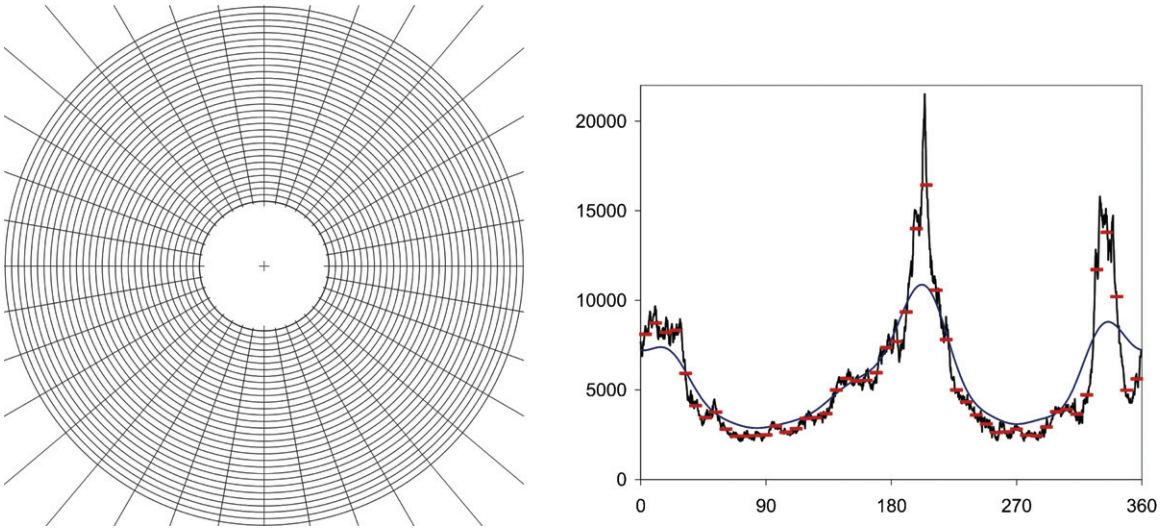

Figure 1. Illustration of the computation of the FNRGF. Panel (a) shows an image being split in circles and angular segments. The figure is simplified in the sense that in practice the annuli are only one pixel wide and there are more angular segments. Panel (b) documents the computation. The black line represents original image values, red bars represent the averages in each of the segments, and the blue line is a Fourier approximation of these averages with attenuation parameters set to $A_0 = 1$, $A_1 = 0.9$, $A_2 = 0.8$,..., $A_{10} = 0$.

Kienreich et al. (2009), Lugaz et al. (2009), and Frazin et al. (2009).

In this work, we present a new filter called the Fourier normalizing-radial-graded filter or the FNRGF, inspired by the NRGF and described in Section 2. Results of its application to the total solar eclipse observations of 2010 July 11, described in Habbal et al. (2011), and to data from space-borne observations are given in Section 3. An improvement to the technique which deals with additive noise is described in Section 4.1. A comparison with other methods is presented in Section 4.3, and a discussion on the various parameters which affect the results is given in Section 4.2.

2. THE FOURIER NORMALIZING-RADIAL-GRADED FILTER

Let X be an unprocessed image of the solar corona where the pixel values are directly proportional to the brightness of the corona at that location. X will be referred to in what follows as the original image, which has a linear dependence on coronal brightness. The pixels of the image can be described either with Cartesian coordinates (x, y) or with heliocentric polar coordinates (r, ϕ).

The NRGF introduced by Morgan et al. (2006) removes the steep radial gradient in images of the solar corona by subtracting the average of X (denoted by $\mathrm{E}X(r)$) and then dividing by the standard deviation (square root of the variance of X denoted by $\mathrm{D}X(r)$) computed along concentric circles around the Sun, i.e., the resulting image Y is computed as

$$Y(r, \phi) = \frac{X(r, \phi) - \mathrm{E}X(r)}{\sqrt{\mathrm{D}X(r)}}. \quad (1)$$

This approach applies the same transformation on all pixels in each circle. Therefore, it cannot compensate for different contrast of structures at the same height. The FNRGF filter presented in this work compensates for that in a way described below.

The FNRGF is an advanced filter based on the NRGF. It splits the image into tens of non-overlapping angular segments, which we index $s = 0, 1, \ldots, n-1$. This is illustrated schematically in Figure 1(a). For each height r and each angular segment the average pixel value and standard deviation is calculated. This process results in two sequences of values as a function of angle ϕ at each height—the average and the standard deviation. These functions are then approximated by a tenth-order Fourier series, with suitable attenuation factors used for the higher order terms (see Section 4.2). Approximation by the Fourier series was selected due to its periodicity. An example of the original values and the Fourier series approximation is shown in Figure 1(b). Finally, each pixel in the image can be processed by subtracting the Fourier approximation of the mean and dividing by the Fourier approximation of the standard deviation, at the particular height and angle of that pixel. The method can be described by the following formulae:

$$a_{r,0} = \frac{2}{n} \sum_{s=0}^{n-1} \mathrm{E}_s X(r), \quad (2)$$

$$a_{r,k} = \frac{2}{n} \sum_{s=0}^{n-1} \mathrm{E}_s X(r) \cos \frac{2\pi k(s + 0.5)}{n} \quad k = 1, 2, \ldots, 10, \quad (3)$$

$$b_{r,k} = \frac{2}{n} \sum_{s=0}^{n-1} \mathrm{E}_s X(r) \sin \frac{2\pi k(s + 0.5)}{n} \quad k = 1, 2, \ldots, 10. \quad (4)$$

Coefficients $a_0, a_1, \ldots, a_{10}, b_1, \ldots, b_{10}$ are coefficients of the Fourier series of the function given by values of the mean in each segment $\mathrm{E}_s X(r)$ at each height r. Integrals are computed numerically by means of the trapezoidal rule. Coefficients $c_0, c_1, \ldots, c_{10}, d_1, \ldots, d_{10}$ are computed for the standard deviation σ in a similar way. The attenuated Fourier approximations of the mean and the standard deviation in each pixel are computed as

$$F_{\mathrm{E}}(r, \phi) = A_0 \frac{a_0}{2} + \sum_{k=1}^{10} A_k (a_{r,k} \cos k\phi + b_{r,k} \sin k\phi), \quad (5)$$

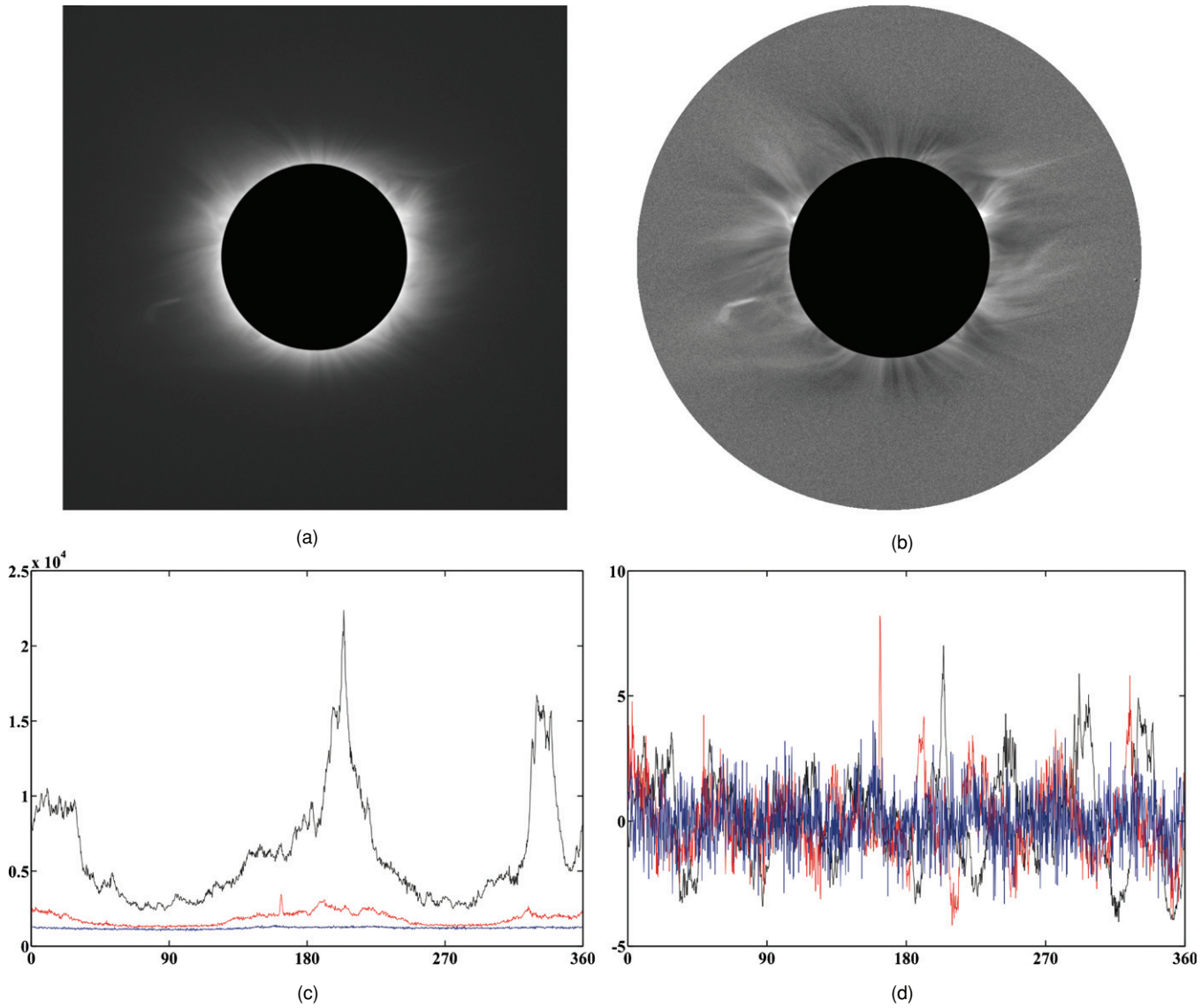

Figure 2. (a) Original Fe x 637.4 nm image shown with a logarithmic brightness scale. (See Habbal et al. (2011) for details of the eclipse observations.) (b) Image (a) after the application of the FNRGF. (c) and (d) Latitudinal profiles of images (a) and (b) at heights of 1.3 (black), 1.6 (red), and 2.2 $R_\odot$ (blue).

$$F_\sigma(r,\phi) = S_0\frac{c_0}{2} + \sum_{k=1}^{10} S_k(c_{r,k}\cos k\phi + d_{r,k}\sin k\phi), \quad (6)$$

with attenuation parameters $A_0, \ldots, A_{10}, S_0, \ldots, S_{10} \in \langle 0, 1\rangle$. The series of A_k and the series of S_k should be non-increasing. Finally, the filtered image Y is computed as

$$Y(r,\phi) = \frac{X(r,\phi) - F_E(r,\phi)}{F_\sigma(r,\phi)}. \quad (7)$$

To preserve some information about the absolute brightness of image X, image Y can be then combined with the original image to create image $Z = K_1 \cdot X + K_2 \cdot Y$, where K_1 and K_2 are non-negative numbers which control the weighting between the original and processed image. The FNRGF was first implemented in Borland Delphi and will soon be available in IDL as part of the Solar Software CORIMP package.

3. RESULTS

3.1. Application to Total Solar Eclipse Observations

All examples in this article are drawn from the eclipse observations of 2010 July 11 made in white light and a suite of Fe emission lines (see Habbal et al. 2011 for details of the experimental setup and the observations). Figure 2 illustrates the result of the application of the FNRGF to an Fe x 637.4 nm image. Since accurate knowledge of the Sun's geometry within the image is critical to the operation of the FNRGF, details of how the Sun center position was calculated are given in the Appendix. Figure 2(a) shows how the observation is dominated by the steep decrease of brightness—only the very innermost corona can be seen, and there is no appreciable structural detail. The FNRGF compensates for this decrease by subtracting the Fourier-approximated local average of pixel values, as shown in Figure 2(b). The latitudinal profiles of the original observation shown in Figure 2(c) clearly demonstrate that the variability of the observed brightness is decreasing sharply—that is, not only is the average brightness decreasing, but the variability is

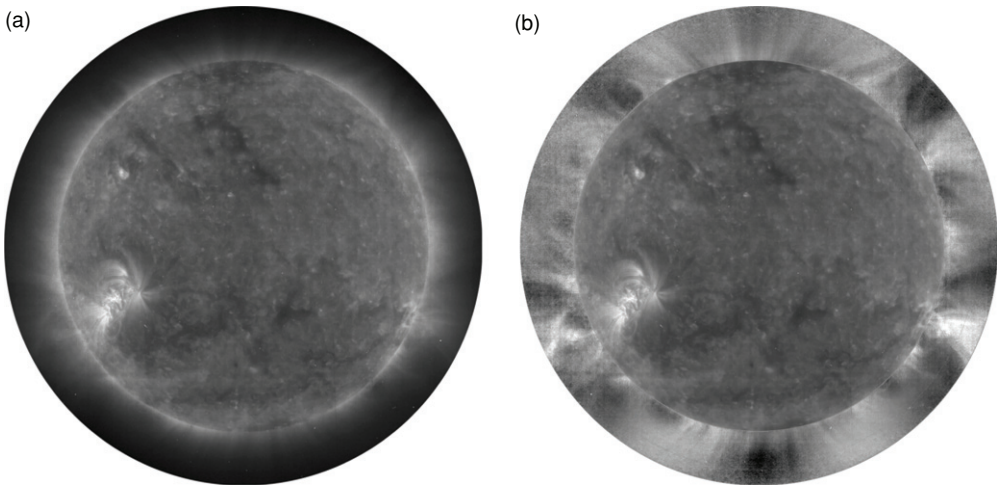

Figure 3. (a) EIT 195 Å observation taken at 2010 July 11 18:54, close to the time of the total solar eclipse. The off-limb field of view is cropped to 1.3 $R_{\odot}$. (b) The same image with off-limb regions processed with the FNRGF to enhance structural detail.

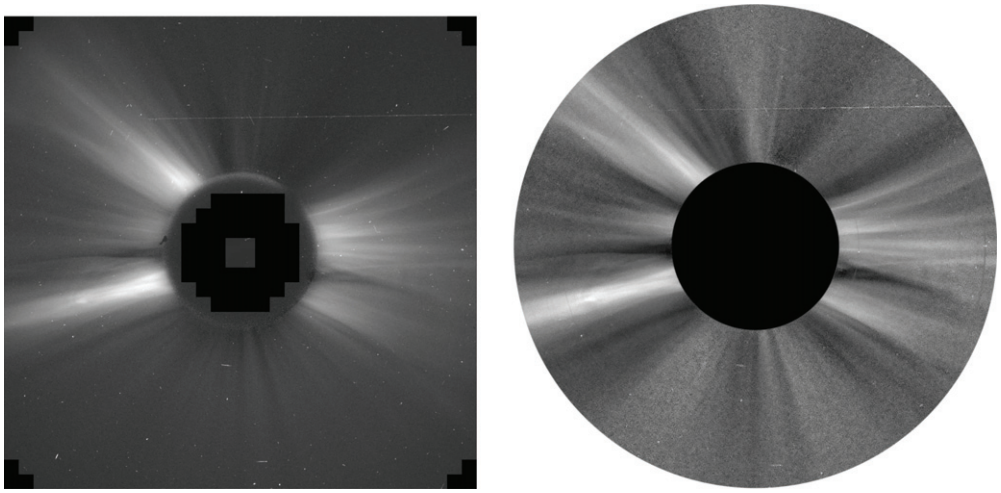

Figure 4. (a) LASCO/C2 white light brightness observation taken at 2011 July 11 22:06. The inner limit of the field of view is ∼2.2 $R_{\odot}$, as dictated by the occulting disk. The outer field of view extends to ∼6 $R_{\odot}$ at the center of the image edges. (b) The same image processed with the FNRGF.

also decreasing. The FNRGF compensates for this decrease by dividing by the Fourier-approximated local standard deviation of pixel values. Thus, structures further from the Sun are enhanced much more than those close to the disk. This is shown in the latitudinal profiles of Figure 2(d). The structural details which are observed in eclipse images are very effectively revealed by the FNRGF processing, as demonstrated by the clarity of Figure 2(b).

3.2. Application to Space-based Observations

The value of the FNRGF is of course not limited to eclipse images. We show here how the application of this tool significantly improves the depiction of coronal structures in coronagraph and EUV images.

Figure 3 shows the application of the FNRGF to an observation from the EUV Imaging Telescope (EIT) aboard the *Solar and Heliospheric Observatory* (Delaboudiniere et al. 1995), which observes the chromosphere and low corona in collisionally excited emission lines of highly ionized iron. The 195 Å bandpass is dominated by Fe XII emission at a peak formation temperature around 1.5 MK. In Figure 3, we show an image taken in this bandpass five minutes after the eclipse observations. The outer part of the image was processed by means of FNRGF to enhance details in the solar corona. Before applying the filter, impulse noise (for example, faulty pixels, or hits of the sensor by high-energy particles) was filtered out from the original picture by means of a simple point filter. The image reveals fine-scale structures in the innermost corona, as well as their connections to structures on the solar disk, which were invisible in the original image.

Figure 4 shows an application of the FNRGF to a white light image taken by the Large Angle and Spectrometric Coronagraph (LASCO) C2 coronagraph (Brueckner et al. 1995) at the time of the eclipse observations. A significant amount of impulse noise was filtered from the image before application of the FNRGF. Since FNRGF subtracts the local average of brightness, it enhances structures in darker polar regions, thus revealing polar plumes at all heights within the field of view. These would otherwise remain invisible—even with NRGF processing. Other interesting structural details are revealed in the equatorial streamer region.

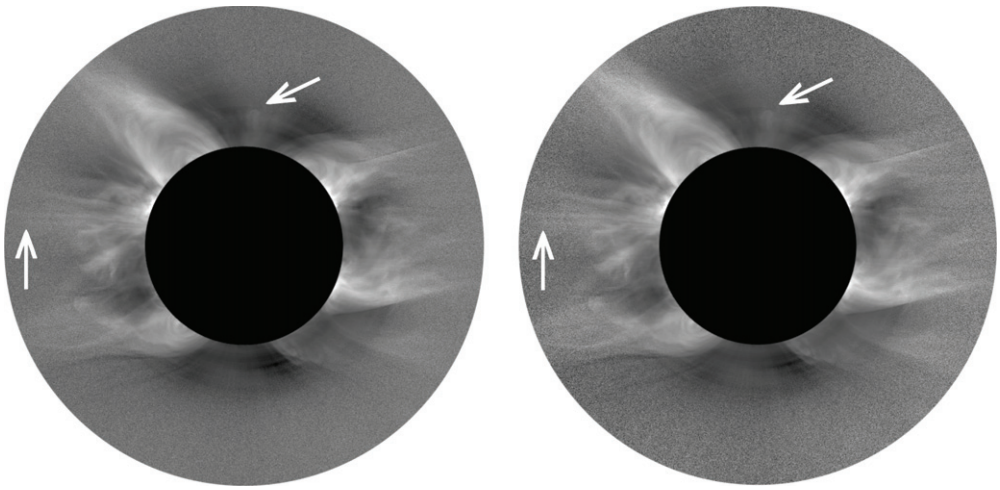

Figure 5. Comparison of the Fe XIV 530.3 nm eclipse image processed with (a) FNRGF and (b) FNRGF-N with parameter m set to 0.5 (see the text). The arrow near the north pole points to a localized enhancement which is better revealed in the FNRGF-N image. The arrow above the east limb points to two rays which extend to greater heights in the FNRGF-N image.

4. DISCUSSION

4.1. FNRGF with Compensation of Additive Noise

When the standard deviation is computed using the FNRGF, it is computed from the values of the original image. Like every image, this image contains additive noise, i.e., image X is a sum of two components, the signal U and the noise N, i.e., $X = U+N$. Since we are working with a linear image, the additive noise is independent of the signal. These two components can be thought of as realizations of two independent random variables. In probability theory, if A and B are two independent random variables with finite first and second moments, and their sum $C = A + B$ (also a random variable), it holds that their mean denoted by $\mathrm{E}Z$ where Z represents a random variable, and variance $\mathrm{D}Z$ are such that

$$\mathrm{E}C = \mathrm{E}A + \mathrm{E}B, \quad \mathrm{D}C = \mathrm{D}B + \mathrm{D}A. \tag{8}$$

(For details see e.g., Williams 2001). Since $X = U+N$, the same applies to the variances $\mathrm{D}X = \mathrm{D}U + \mathrm{D}N$. If we have a method to estimate the variance $\mathrm{D}N$ of the noise in image X, we can compute the variance of the ideal image as $\mathrm{D}U = \mathrm{D}X - \mathrm{D}N$. A method described by Jaroslavskij & Bajla (1989), based on the covariance of shifted images, can be used to estimate the noise variance. The method was applied to the eclipse images with poor results. The steep radial gradient of brightness close to the solar disk and lack of information further from the disk made this method unsuitable. However, if there is a region in the original image which contains a uniform coronal structure or no structure at all and the decrease of brightness is negligible there, the variance of the pixels in this region can be used as an estimation of the noise variance.

As shown in Figure 2(d), the structures close to the solar disk continue to have higher contrast than those far from the Sun, even after the application of the FNRGF. This is caused by the fact that FNRGF, as described in Section 2, divides by the local standard deviation without consideration of noise. Even though additive noise is approximately constant throughout the image, the signal-to-noise ratio decreases sharply with distance from the Sun. Therefore, the calculated standard deviation becomes increasingly dominated by the noise with increasing height. This is undesirable—what is needed is a reliable estimate of the standard deviation due to different coronal structure, not influenced by noise. That is, all structures in the processed images would have the same contrast at all heights if we were dividing by the standard deviation of the ideal image U contained in image X, without inclusion of $\mathrm{D}N$. Unfortunately, simply using $\sqrt{\mathrm{D}X - \mathrm{D}N}$ (or rather $\sqrt{\mathrm{D}X - m\mathrm{D}N}$ with $m \in \langle 0, 1)$) instead of $\sqrt{\mathrm{D}X}$ in the FNRGF process caused the attenuation parameters (discussion on these parameters is provided in Section 4.2) to be set too low to obtain an acceptable image. However, subtracting the estimated noise standard deviation from the measured local standard deviation proved to work. The formula for FNRGF with additive noise compensation, which for convenience we rename FNRGF-N, is then

$$Y(r, \phi) = \frac{X(r, \phi) - F_{\mathrm{E}}(r, \phi)}{F_{\sigma}(r, \phi) - m\sqrt{\mathrm{D}N}} \tag{9}$$

with $m \in \langle 0, 1)$. This allows higher enhancement in regions of lower contrast than the original FNRGF. The enhancement of the most prominent structures is about the same with FNRGF and FNRGF-N, while the fainter structures are better enhanced with the FNRGF-N.

A comparison of the results of FNRGF and FNRGF-N is shown in Figure 5. In principle, the FNRGF-N enhances noise, but its enhancement of faint coronal structures is better than that of the FNRGF. One practical difficulty of the FNRGF-N is the necessity of finding a region which contains no structure, that is, a region where the brightness gradient is negligible, in order to calculate the noise contribution. In the case of Figure 5, an appropriate square region of size 50×50 pixels was chosen. The region was at a large height within a coronal hole and, from its uniform appearance, contained no coronal structure. Improvements in enhancement of fine structures especially in regions of lower contrast can be observed. For example, the arrows at the polar region point to a localized enhancement which is better revealed in the FNRGF-N image. The arrows on the east point to two rays which are seen to extend further in comparison with the FNRGF image. On the other hand, additive noise is enhanced more in the FNRGF-N image.

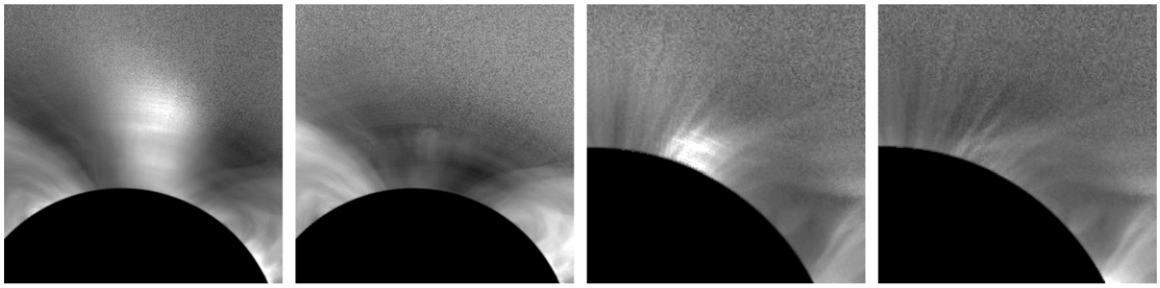

Figure 6. Illustration of suitable and unsuitable setting of attenuation parameters, using the 2010 total solar eclipse observations of (a) and (b) Fe XIV emission, and (c) and (d) Fe X emission. The attenuation parameters for the average are too high in (a), but are close to optimal in (b). Similarly, the parameters for the standard deviation are too high in (c) and are close to optimal in (d).

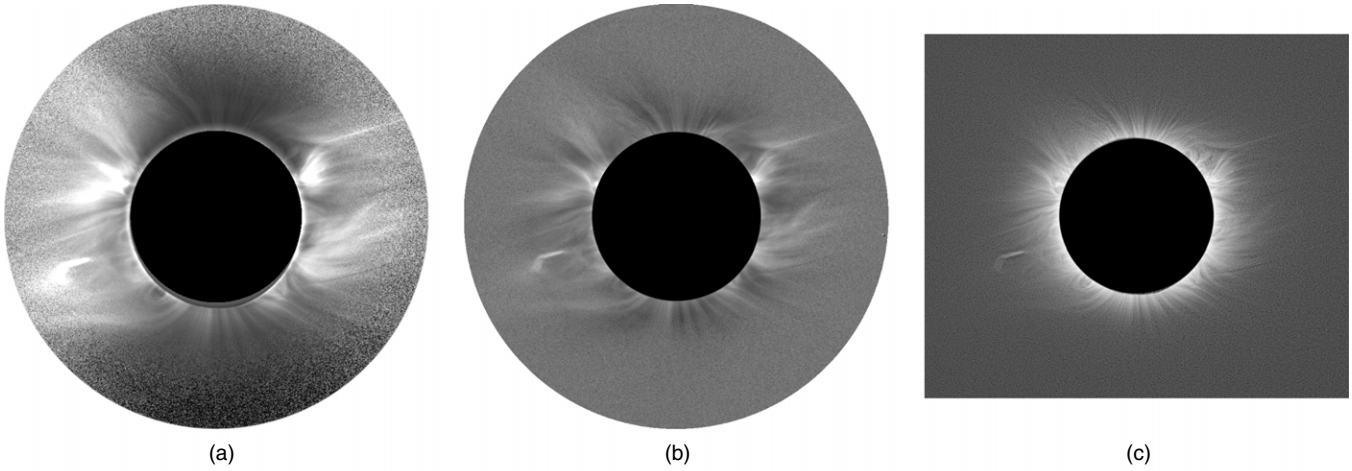

Figure 7. Fe X eclipse image processed with (a) NRGF, (b) FNRGF, and (c) ACHF.

4.2. Discussion of the Values of the Parameters

As with any image processing technique, the choice of various parameters affects the outcome of the final processed image. This section describes how a careful choice of the various parameters which control the FNRGF yield the best result for revealing coronal structure.

The images processed by the FNRGF and presented here were created with $n = 50$ angular segments. The number must be much higher than the number of Fourier coefficients involved in the filter, which is 21 if the Fourier series is computed up to the tenth order.

The values of the multiplication factors K_1 and K_2 depend on the range of pixel values of the original image. It is their ratio rather than their values that affects the result. The original image X may have any range of pixel values $\langle p, P\rangle$ typically with $p = 0$, whereas the filtered image Y has pixel values independent of the range in the original image. The FNRGF normalizes the pixel values in the image, i.e., the average pixel value in image Y is close to zero and the range Q of its pixel values q is symmetric around zero (Q is close to $-q$). Therefore, if we want to process two original images X_1 and X_2 in the same manner, factors K_2 should be the same for both images. Factors K_1 for these images, i.e., $K_{1,1}$ and $K_{1,2}$, should be normalized in the sense that

$$K_{1,1} \cdot (P_1 - p_1) = K_{1,2} \cdot (P_2 - p_2), \tag{10}$$

where p_1, p_2 are minimal pixel values in the original images X_1, X_2 and P_1, P_2 are their maximal values. Alternatively, a more robust statistical characteristic such as the difference between the 0.95-quantile and the 0.05-quantile of image pixel values can be used for the normalization of factors K_1 instead of the pixel value range $P-p$. For example, in Figure 2(b), the multiplication factors were set to $K_1 = 1$, $K_2 = 15{,}000$, while the pixel values in the original image varied from 0 to 514 040.

There are 22 attenuation parameters in total involved in the filter, 11 parameters $A_0, \ldots, A_{10}$ for the average and 11 parameters $S_0, \ldots, S_{10}$ for the standard deviation. Setting $A_0 = S_0 = 1$ and all other parameters equal to zero is equivalent to the NRGF. Each sequence of the attenuation parameters should not increase to obtain an image with a monotone modulation transfer function, that is, higher order components should have smaller or equal attenuation parameters than lower order components. To obtain filtered images with the average pixel value equal to 0, the parameter A_0 should be set to 1. The setting of the other parameters depends on the signal-to-noise ratio in the original image and on the distribution of structures around the solar disk. If the parameters are too low, the coronal structures are enhanced less than they could be.

Figure 6 illustrates the effects of setting parameters too high. The two examples show Fe X 637.4 nm and Fe XIV 530.3 nm eclipse images, when striking artifacts arise from the careless choice of parameters. If the parameters for the average are too high, the periodicity of sine and cosine functions in the Fourier series causes erroneous brightenings or darkenings in some regions. Both Figures 6(a) and (b) have the same setting of the standard deviation attenuation parameters. In Figure 6(a), the average attenuation parameters are all set to 1, whereas in Figure 6(b), they are $A_0 = 1$, $A_1 = 0.85$, $A_2 = 0.7$, $A_3 = 0.55$, $A_4 = 0.4$, $A_5 = 0.25$, $A_6 = 0.1$, $A_7 = \ldots = A_{10} = 0$. Suitable

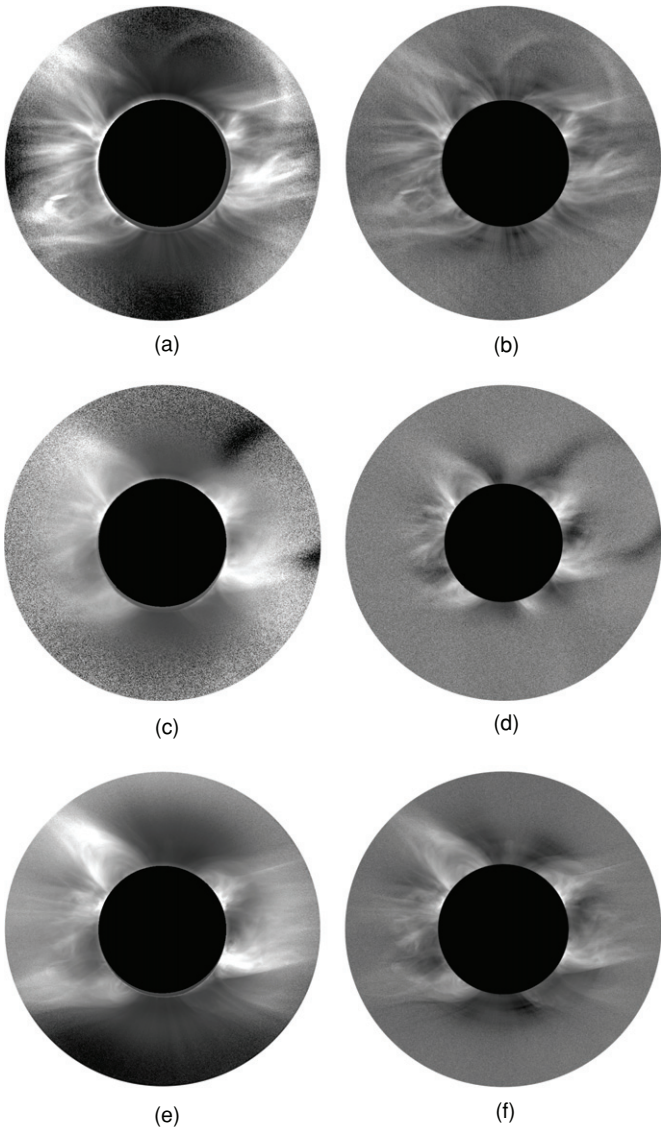

Figure 8. Eclipse images of the coronal forbidden lines processed with NRGF (left column) and FNRGF (right column). The emission lines are (a, b) Fe XI 789.2 nm, (c, d) Fe XIII 1074.7 nm, and (e, f) Fe XIV 530.3 nm.

values of these parameters depend sensitively on the distribution of the coronal structures. It would not be necessary to attenuate the average as much at times of maximum solar activity because the coronal structures would be evenly distributed around the solar disk and therefore the higher order terms of the Fourier series would be lower.

If the parameters for the standard deviation are too high, they make the Fourier series oscillate too much and at some places the Fourier approximation of the standard deviation can become close to zero. This brings about a very high relative enhancement rate resulting in extremely bright or extremely dark places. This is illustrated in Figures 6(c) and (d). The difference between the parameters in these two images is quite small, in Figure 6(c), they are $S_0 = 1$, $S_1 = 1$, $S_2 = 0.9$, $S_3 = 0.8$, $S_4 = 0.7$, $S_5 = 0.6$, $S_0 = 0.5$, $S_7 = \ldots = S_{10} = 0$ whereas in Figure 6(d), they are $S_0 = 1$, $S_1 = 0.9$, $S_2 = 0.8$, $S_3 = 0.7$, $S_4 = 0.6$, $S_5 = 0.5$, $S_6 = 0.4$, $S_7 = \ldots = S_{10} = 0$. A general rule for setting the standard deviation attenuation parameters is that images with sharper edges require lower values of the parameters. The reason for this rule is that sharp edges cause stronger higher order terms in the Fourier series.

The parameter m is introduced in Equation (9). It compensates for the fact that the standard deviation due to noise becomes stronger relative to the standard deviation due to coronal structure with height. Setting a value for m is straightforward since it depends on the measureable value of signal-to-noise ratio in low-contrast regions. It should therefore be included in the procedure. However, within sensible limits, FNRGF-N is rather insensitive to the value of m. $m = 0$ is equivalent to the original NRGF. Very high values of m may cause artifacts similar to those caused by high values of the standard deviation attenuation factors.

If the FNRGF-N procedure is to be used as a batch process on many images, the attenuation parameters and parameter m have to be low enough to suit all the images. The automated setting of the attenuation parameters will be the subject of a future study.

4.3. Comparison with Other Methods

Figure 7 compares the application of three different image processing techniques to the Fe X observation shown in Figure 2. Figure 7(a) shows the application of the NRGF (Morgan et al. 2006), Figure 7(b) the FNRGF (this work), and Figure 7(c) the ACHF (Druckmüller et al. 2006). The NRGF processing subtracts an average, and applies a constant contrast enhancement, along Sun-centered circles. While this is effective in removing the average radial gradient in brightness, it does not offer a way to enhance finer structural details in the azimuthal direction. For example, faint plumes in the coronal holes still appear faint since they are contrast-enhanced alongside the very bright streamers. This deficiency is overcome using the FNRGF, which is adaptive in the azimuthal direction as well as the radial direction. For example, plumes appear far more clearly in the FNRGF image compared to the NRGF. The ACHF method uses a specific class of unsharp masks. Unlike the other two processes, it does not only use neighboring pixels lying on each circle, it also uses pixels on circles closer and further from the Sun. ACHF enhances finer details than both the NRGF and FNRGF, since it uses several unsharp masks starting from high spatial frequencies to enhance different frequencies. In contrast to the ACHF, images processed with the FNRGF often do not make use of the full resolution of the images. On the other hand, due to their insensitivity to absolute brightness and absolute contrast, both the NRGF and FNRGF techniques enhance faint structures at larger heights compared to the ACHF. The noise compensation method is a development which further improves the FNRGF processing in regions of lower contrast. In summary, the FNRGF is an improvement on the NRGF due to its ability to bring out fainter structural details, and is less suspect to noise and absolute brightness contrast than the ACHF.

Increasing the Fourier order in the FNRGF filter may enhance finer structural detail. However, as discussed in Section 4.2, this can introduce unwanted artifacts if one is not careful. Tests on the examples presented in this article show that the use of higher-order Fourier series terms does not necessarily give desirable results.

Since the NRGF subtracts the average along whole Sun-centered circles, it preserves the information on the relative brightness of the corona along each circle, i.e., coronal holes above the poles remain dark and bright streamers remain bright. This information is suppressed in images processed with FNRGF and almost completely lost in images processed with ACHF. While this is useful to reveal fine structure within all

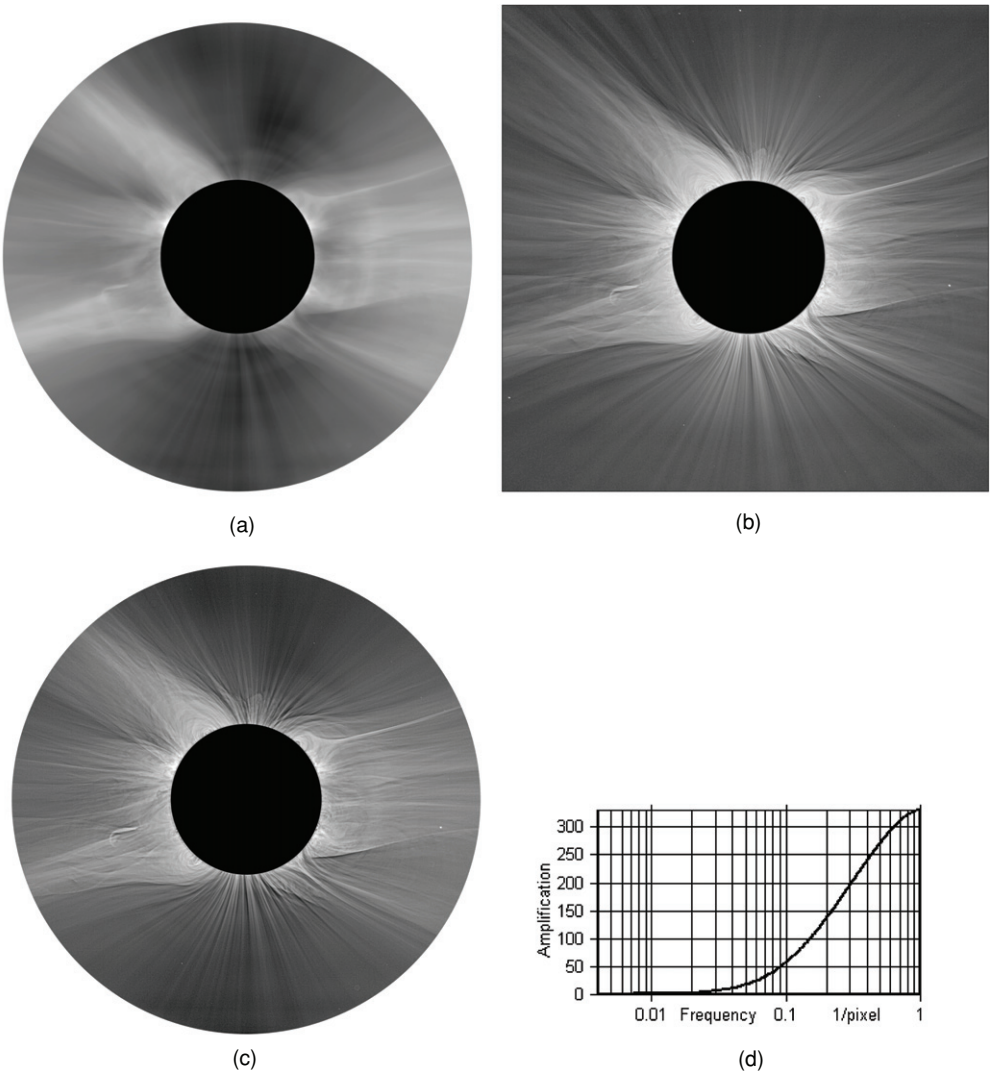

Figure 9. White light image of the 2010 total solar eclipse processed by (a) FNRGF and (b) the ACHF. (c) The weighted sum of panel (a) and small-scale structures from panel (b) as described in the text. (d) The relative amplification of coronal structures as a function of spatial frequency—the radius of the Sun is 275 pixels.

regions, it can result sometimes in a loss of context since dark regions are set on a par with bright structures. Lower settings for higher order FNRGF attenuation parameters, especially for the average, can make the resulting pictures closer to the NRGF and keep the information on the relative brightness along Sun-centered circles. The ACHF is most suitable for viewing very fine detail, but does not help the eye in distinguishing between what was originally high brightness streamers and low brightness coronal holes. In summary, the NRGF or FNRGF preserve more of the original large-scale detail.

A comparison of the coronal forbidden line eclipse images, processed with the NRGF and the FNRGF, is shown in Figure 8. This comparison illustrates how the FNRGF is more effective at enhancing higher-frequency structures, and structures in regions of lower contrast—in particular the extensive polar regions—compared to the NRGF. Examples of these differences can be seen almost everywhere in these images. The most obvious differences are in the polar plumes in the north in Figures 8(a) and (b) and in the eastern equatorial region in Figures 8(e) and (f).

As a final example, we compare a white light eclipse image processed with both FRNGF and ACHF. This is shown in Figures 9(a) and (b). The comparison shows that ACHF is able to enhance much smaller details than FNRGF. In the example shown, the observed signal is very high even to extended heights in the corona. This enables the ACHF to enhance fine structural details out to several solar radii. In many coronal images, particularly in narrowband emission line images of the extended corona, and in coronagraph images taken outside an eclipse, the signal to noise becomes low, even at small heights. In such images, the FNRGF is a more viable option for revealing structure than the ACHF.

4.4. Combination of FNRGF and ACHF

A practical consideration is the computational time taken to process the images. On a standard desktop computer, the FNRGF image in Figure 9(a) takes a few minutes, whereas the ACHF image in Figure 9(b) takes several hours. A more recent implementation of FNRGF written in IDL reduces the computational time considerably—to the order of seconds. Computation of masks for the enhancement of large-scale structures in the ACHF takes a majority of the computing time. Since FNRGF enhances larger-scale structures very efficiently, a

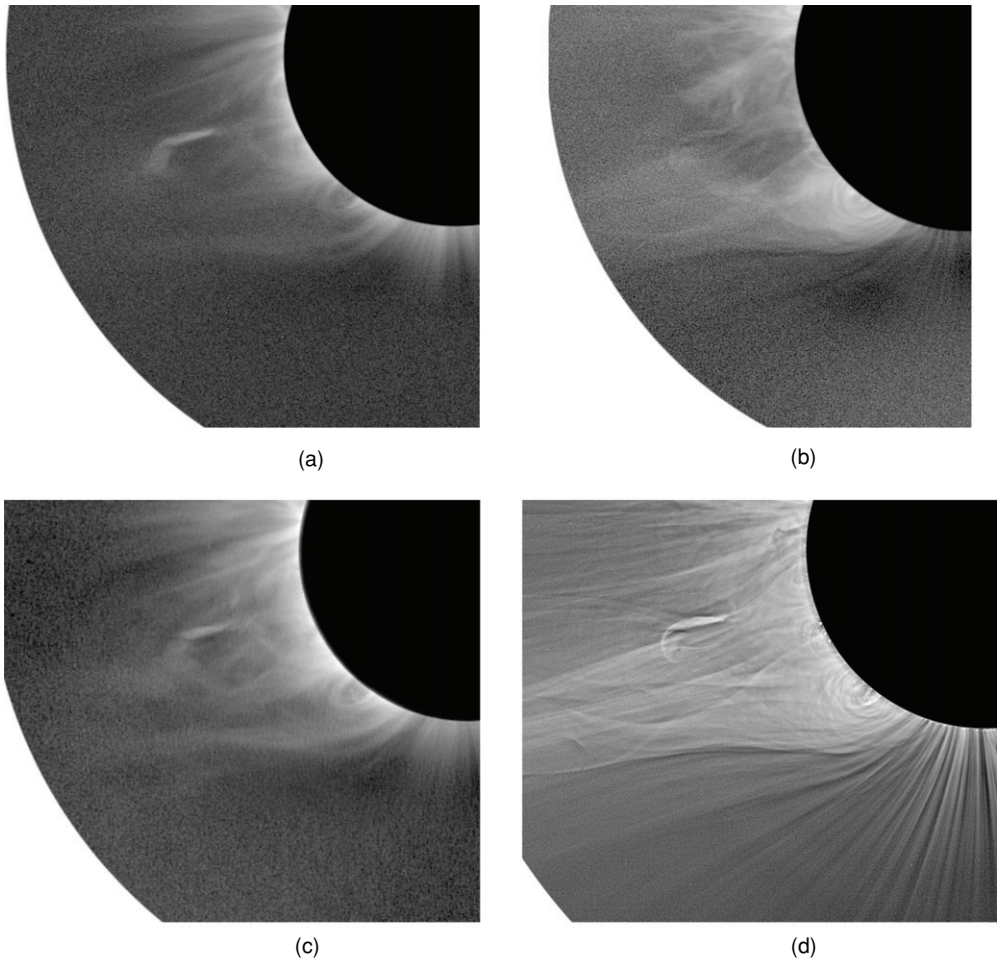

Figure 10. (a) Fe x, (b) Fe xi, (c) Fe xiv, and (d) white light eclipse images showing details of the southeast corona. The images are weighted sums of images processed with the FNRGF and ACHF, using a ratio of 4 : 6. Most striking in this example are the differences in the details of structures observed in each spectral line (a–c) and in white light (d). Such differences are attributed to the different temperatures of the fine structures, as depicted in Fe x (0.8 MK), Fe xi (1.16 MK), and Fe xiv (1.8 MK) and the electron-scattered component (panel d).

combination of both methods can produce images with enhanced structures of all sizes computed in a time which is more than an order of magnitude shorter than the computing time of ACHF. Figure 9(c) shows an image created by the described method. It is a weighted average of 0.4 of the FNRGF image shown in Figure 9(a) and 0.6 of the high frequencies of the ACHF image shown in Figure 9(b). The relative enhancement of small-scale structures used for the creation of image in Figure 9(c) is described by Figure 9(d). In this plot, the relative amplification of coronal structures at various spatial scales is shown. Large spatial scales are attenuated while small scales are amplified considerably. Figure 9(c) is a spectacular image computed in a short computing time of several minutes on a common desktop computer.

The combination of FNRGF and ACHF used for the production of Figure 9(c) can also be used for observations of the spectral lines presented in Figure 8. These images processed with the ACHF by M. Druckmüller were published in Habbal et al. (2011). Figure 10 is an example of this combination for a section of the corona, for three spectral lines and white light eclipse observations. The images are weighted averages of 0.4 of images processed with the FNRGF and 0.6 of images processed with the ACHF. The resulting images, which take advantage of the properties of both methods, show the structures in the emission of coronal forbidden lines in exceptionally high quality, with the high-frequency structures revealed by the ACHF and the larger-scale structures extending further away from the Sun as a consequence of the FRNGF. We note in particular the "hook-like" feature off the east limb. This feature is the residual of the passage of a prominence eruption and a CME several hours prior to the eclipse observations. The Fe xi emission, with a peak ionization temperature of 1.1 MK (Figure 10(b)) shows how the "hook" is still connected to the solar disk and together with the Fe xiv emission with a peak ionization temperature of 1.8 MK (Figure 10(c)) show a faint envelope to this whole structure. The intricate structure of this residual of the passage of the CME remains hidden in images processed with other methods (see, for example, Habbal et al. 2011). Due to the use of images processed with ACHF, images in Figure 10 show the loops surrounding the prominence on the southeast limb of the Sun very well, and the use of FNRGF-processed images enhances the connecting structures further from the Sun.

5. CONCLUSION

We presented in this work a new FNRGF for the enhancement of structures in solar coronal images. The filter reduces the dominance of the steep radial gradient of brightness and the contrast between bright and faint structures in these images. The resulting images enable us to study both low- and high-

frequency structures in broadband or narrowband emission line images. The method is computationally fast, typically taking only a few seconds to process a 1K×1K image on a standard desktop computer. The processed images help to interpret structures present in the original calibrated data. In particular, they provide the context for further analysis of the information pertaining to plasma parameters embedded in the data. When compared with images processed with the NRGF, the FNRGF visualizes finer details, especially in regions of lower contrast. While the NRGF and FNRGF are based on a completely different principle than the ACHF, the latter enhances finer details than NRGF and FNRGF. A proposed combination of the FNRGF and ACHF takes advantage of both these methods. In relatively short computing times, this combined method enhances high-frequency structures of the corona as well as lower-contrast structures further away from the Sun, giving us new possibilities to study the intricate structures of the inner corona.

The authors thank Professor Miloslav Druckmüller for providing the calibrated eclipse data and for constructive discussions. H. Druckmüllerová thanks members of the Institute for Astronomy for their hospitality during her visit when this work was completed. This work was supported by NASA grants NNX07AH90G and NNX08AQ29G to the Institute for Astronomy of the University of Hawaii, and grant 205/09/1469 of the Czech Science Foundation.

APPENDIX

DETERMINING THE SUN CENTER IN TOTAL SOLAR ECLIPSE IMAGES

If we are processing a composite of images taken during a total solar eclipse, the center of the Sun (H_x, H_y) can be determined from the position of the Moon and the geometrical parameters of the eclipse computed using appropriate ephemeris and/or a standard eclipse calculator from the coordinates of the observing site. Let M_E be the radius of the Moon in image pixels, and R_{MS} be the ratio of the Moon radius to the Sun's computed by an eclipse calculator. The radius of the Sun H_R is then $H_R = M_E/R_{MS}$. Let B be the umbral depth of the observing site. This number is given in percent and is multiplied by (-1) if the site is to the north of the central line. This value is converted into a number $h \in \langle -0.5, 0.5\rangle$ with 0 on the central line, -0.5 on the northern edge, and 0.5 on the southern edge of the path of totality, i.e., if $B < 0$ then $h = -0.5 - N/200$, otherwise $h = 0.5 - B/200$. After images are registered so that the Sun is kept at a constant position (e.g., by means of the modified phase correlation described in Druckmüller (2009), the motion of the Moon within the image can be described by the numbers $M_{x,0}$, $M_{y,0}$, M_{dx}, M_{dy} such that at any time t the position of center of the Moon is $M_x = M_{x,0} + t \cdot M_{dx}$, $M_y = M_{y,0} + t \cdot M_{dy}$ with $(M_{x,0}, M_{y,0})$ being the position of the center of the Moon at the time of the second contact. If l is the duration of the total eclipse in seconds then the position of the center of the Sun (H_x, H_y) in the images is computed as follows:

$$\delta = 2h(M_E - H_R) \tag{A1}$$

$$\begin{aligned} n_x &= M_{dx} \\ n_y &= -M_{dy} \end{aligned} \quad \text{a normal to the motion of the Moon pointing to the solar north} \tag{A2}$$

$$v = \sqrt{n_x^2 + n_y^2} \tag{A3}$$

$$\begin{aligned} n_{\delta,x} &= \delta \frac{n_x}{v} \\ n_{\delta,y} &= \delta \frac{n_x}{v} \end{aligned} \quad \text{the normal with length changed to } \delta \tag{A4}$$

$$H_x = M_{x,0} + \frac{l}{2} M_{dx} + n_{\delta,x} \tag{A5}$$

$$H_y = M_{y,0} + \frac{l}{2} M_{dy} + n_{\delta,y} \tag{A6}$$

REFERENCES

Brueckner, G. E., et al. 1995, Sol. Phys., 162, 357
Byrne, J. P., Gallagher, P. T., McAteer, R. T. J., & Young, C. A. 2009, A&A, 495, 325
Delaboudiniere, J.-P., et al. 1995, Sol. Phys., 162, 291
Druckmüller, M. 2009, ApJ, 706, 1605
Druckmüller, M., Rušin, V., & Minarovjech, M. 2006, Contrib. Astron. Obs. Skalnate Pleso, 36, 131
Espenak, F. 2000, in ASP Conf. Ser. 205, Last Total Solar Eclipse of the Millennium, ed. W. Livingston & A. Özgüç (San Francisco, CA: ASP), 101
Frazin, R. A., Jacob, M., Manchester, W. B., Morgan, H., & Wakin, M. B. 2009, ApJ, 695, 636
Habbal, S. R., Druckmüller, M., Morgan, H., Scholl, I., Rušin, V., Daw, A., Johnson, J., & Arndt, M. 2010a, ApJ, 719, 1362
Habbal, S. R., et al. 2010b, ApJ, 708, 1650
Habbal, S. R., et al. 2011, ApJ, 734, 120
He, J., Marsch, E., Tu, C., & Tian, H. 2009, ApJ, 705, L217
Jaroslavskij, L., & Bajla, I. 1989, Metódy a Systémy Číslicového Spracovania Obrazov (Methods and Systems of Digital Image Processing) (Bratislava: Alfa)
Kienreich, I. W., Temmer, M., & Veronig, A. M. 2009, ApJ, 703, L118
Koutchmy, O., Koutchmy, S., Nitschelm, C., Sykora, J., & Smartt, R. N. 1988, in Proc. of the Ninth Sacramento Peak Summer Symp., Solar and Stellar Coronal Structure and Dynamics, ed. R. C. Altrock, 256
Lugaz, N., Vourlidas, A., Roussev, I. I., & Morgan, H. 2009, Sol. Phys., 256, 269
Morgan, H., & Habbal, S. R. 2007a, A&A, 464, 357
Morgan, H., & Habbal, S. R. 2007b, A&A, 465, L47
Morgan, H., & Habbal, S. R. 2010, ApJ, 710, 1
Morgan, H., Habbal, S. R., & Woo, R. 2006, Sol. Phys., 236, 263
Newkirk, Jr., G., & Harvey, J. 1968, Sol. Phys., 3, 321
Owaki, N., & Saito, K. 1967, PASJ, 19, 279
Wang, Y., et al. 2010, ApJ, 717, 973
Williams, D. 2001, Weighing the Odds: A Course in Probability and Statistics (Cambridge: Cambridge Univ. Press)